

Scale Analysis of Short Term Forecast Errors

Iain Davison

MSc MNMAO

University of Reading

August 2006

I confirm that this is my own work and the use of all material from other sources has been properly and fully acknowledged.

Iain Davison

Acknowledgements

Completing this dissertation would not have been possible without the help and support of my supervisors Amos Lawless and Nancy Nichols. I would also to thank Sarah Dance for her help and input over the summer.

Thanks are also due to all the staff at the Met Office who allowed me to work on my dissertation there. In particular I wish to thank Gordon Inverarity whose guidance was invaluable.

I would like to acknowledge the NERC for funding this work, without which I would have been unable to complete the course. I would also like to thank the Met Office for funding my time in Exeter, while working on this project.

I would like to say thanks to my parents for their support during my time at university and to my girlfriend Lucy for keeping me sane over the year.

Abstract

We aim to investigate the convergence of the difference between the forecast and analysis fields during the incremental 4D-Var method used in numerical weather prediction at the UK Met Office. We transform the analysis increment into Fourier space in order to look at how the power at each mode number, which is inversely proportional to the wavelength, evolves through the 4D-Var minimisation iterations. We investigate appropriate ways to display results, including power spectra and periodograms and we look at how to use windowing and binning in order to improve the accuracy of the periodogram estimation. Then we compare the results obtained to show that they correspond to those of previous work using the simple barotropic vorticity equation model. We conclude that the largest and smallest scales converge the fastest, after only 10 iterations, while the intermediate scales appeared still to be converging after 30 iterations of the inner loop.

Contents

1	Introduction	3
2	Useful Tools	7
2.1	Discrete Fourier Transforms	7
2.2	The Power Spectrum	11
2.3	The Periodogram	15
2.4	Data Windowing	20
3	The Model and Methodology	24
3.1	Full 4D-Var Assimilation	24
3.2	Incremental 4D-Var Assimilation	26
4	Previous Work on Forecast Error	29
4.1	Four-dimensional Data Assimilation with a Wide Range of Scales	29
4.2	A Validation of the Incremental Formulation of 4D Variational Data Assimilation in a Nonlinear Barotropic Flow	33
5	Numerical Experiments	37
5.1	2D Periodogram	37
5.2	The full 1-D power series scatter plot	41

5.3	The binned 1D periodogram	46
6	Conclusion	51

Chapter 1

Introduction

Four-dimensional variational data assimilation (4D-Var) is a technique used to incorporate observational data into a dynamical model over a given period of time in order to predict all the future and current states of a system [11]. The method aims to minimise the square errors between the observational system data and the model predictions. This can be thought of as minimising a *cost function*, which is a measure of the distance between the model state and the observations, and the model state and the initial state estimate, [10].

The minimisation of the cost function comes at great computational expense. In order to reduce this expense the full minimisation can be approximated by a series of minimisations of approximate convex quadratic cost functions. This approximation to the full 4D-Var method is known as the *incremental* 4D-Var method, [10].

We begin the incremental 4D-Var process with a initial estimate of the field states, known as a *background* field and run the nonlinear model to calculate the field states at each time step. We then calculate the value of

an incremental field, around the background, which minimises an approximately quadratic *incremental cost function*. The minimisation process uses an iterative procedure such as quasi-Newton or conjugate gradient method and is known as the *inner loop*.

The background field is then updated by the addition of the incremental field. The final updated field is called the *analysis* field and can be described as the background field plus the final incremental field. In other words, the incremental field can be thought of as the error between the background and the analysis fields.

This incremental field or *forecast error* contains information of different physical scales. There has been little work published on how these scales evolve and converge throughout the iterative process of the minimisation of the incremental cost function. However, what research there has been, has only been done using simple dynamical models, such as the barotropic vorticity equation on a β -plane approximation, ([15], [9]). It is the aim of this project to analyse the evolution of the physical scales present in the forecast error, using the complicated non-linear model used for numerical weather predictions at the UK Met Office.

To do this we use the operational incremental 4D-Var process on the Met Office nonlinear model. We then study the evolution of the increments as they converge to the final analysis.

One of the motivations we have for studying the evolution of the forecast error is the prospect of using a method known as *multigrid* in order to speed up the iterative process of the inner loop.

The multigrid method is used to solve linear problems, of the form $A\underline{x} = \underline{b}$,

where \underline{x} and \underline{b} are vectors and A is a matrix. This will mean that by describing the gradient of the incremental cost function in this form, we can potentially solve the problem using the multigrid method.

The solution to the multigrid problem is found by eliminating the different components of the error on different resolution grids. High frequency components of the error are eliminated on a high resolution discretisation of the problem, whilst low frequency components are resolved on a coarser discretisation. Solving a problem using multigrid method is done in stages, [13]:

- Presmoothing stage. The high frequency error (relative to the grid being used) are effectively eliminated.
- Restriction stage. The remaining error is transferred to a coarser computational grid, on which we continue to solve the problem.
- Prolongation stage. The correction is then interpolated back onto the finer grid.
- Post-smoothing stage. Any remaining high frequency components are again eliminated.

One iteration by this method, in general, involves descending through a hierarchy of computational grids from finest to coarsest and back up again - a process known as a V-cycle. It is possible to link more than one V-cycle together to introduce further accuracy in the solution.

In order for the multigrid method to be used on the inner loop, we would require the small scale components of the forecast error to be smoothed out quickly so the inner loop can continue on the lower resolution grid. If small

scale errors remain in the problem, then there would be no computational advantage in using a V-cycle of the multigrid method.

To allow the subject matter contained in this project to flow in a way which is easily read and followed, it is laid out in the following way,

- **Chapter 2:** In this chapter we shall look at some tools useful in this project. These include ideas on Fourier transforms, ways to display and analyse the scales present in the forecast error and methods of manipulating and massaging the data.
- **Chapter 3:** This chapter deals with the details of full and incremental 4D-Var assimilation.
- **Chapter 4:** Here we discuss previous work on the evolution of forecast errors. We look at the different methods used and what results were obtained.
- **Chapter 5:** In chapter 5 we analyse the evolution of forecast errors from the Met Office full non-linear model using the incremental 4D-Var assimilation process.
- **Chapter 6:** We summarise the results of the project and form subsequent conclusions that the largest and smallest scales converged the fastest, while the intermediate scales were still to converge at the end of the iterations. This agrees with previous results using the simple barotropic vorticity model used by Tanguay et al. in [15].

Chapter 2

Useful Tools

In this chapter we deal with some tools, used in this project to analyse forecast errors, associated with data manipulation and massaging, such as data windowing and detrending. We also describe ways in which we are able to show the periodicity of a set of sample data by transforming it into Fourier space.

2.1 Discrete Fourier Transforms

Any function defined over a finite domain or any periodic function, $f(x)$, can be defined by expanding it in a series of sines and cosines. From [1] we define the *Fourier Series* of $f(x)$ as

$$f(x) = \frac{a_0}{2} + \sum_{n=1}^{\infty} a_n \cos(nx) + \sum_{n=1}^{\infty} b_n \sin(nx), \quad (2.1)$$

where the coefficients a_0 , a_n and b_n are related to the given function by definite integrals,

$$\begin{aligned} a_n &= \frac{1}{\pi} \int_0^{2\pi} f(t) \cos(nt) dt, \\ b_n &= \frac{1}{\pi} \int_0^{2\pi} f(t) \sin(nt) dt, \quad n = 0, 1, 2, \dots \end{aligned}$$

This is subject to the existence of these integrals, which is true if $f(t)$ is piecewise continuous, [1].

If we now express $\cos nx$ and $\sin nx$, from (2.1), in exponential form, we may rewrite (2.1) as, [1]

$$f(x) = \sum_{n=-\infty}^{\infty} c_n e^{inx}, \quad (2.2)$$

where,

$$\begin{aligned} c_n &= \frac{1}{2}(a_n - ib_n), \\ c_{-n} &= \frac{1}{2}(a_n + ib_n), \quad n > 0 \\ c_0 &= \frac{1}{2}a_0 \end{aligned}$$

The advantage of using a Fourier series in representing a function, over other methods such as a Taylor series, is the ability for it to represent discontinuous functions.

If, however, we require the Fourier series to be evaluated using a digital computer, as in this project, the continuum of values are replaced by a discrete set and therefore integrals are approximated by summation.

We now consider a function of time, $f(t_j)$, measured at discrete time values, $t_j = j\Delta$ where $j = 0, \dots, N-1$ and Δ being the sampling interval. We may construct the *Discrete Fourier Transform*, [1]

$$DFT(f_j) = \tilde{f}_k = \frac{1}{N} \sum_{j=0}^{N-1} f_j e^{-\frac{2\pi ijk}{N}}, \quad (2.3)$$

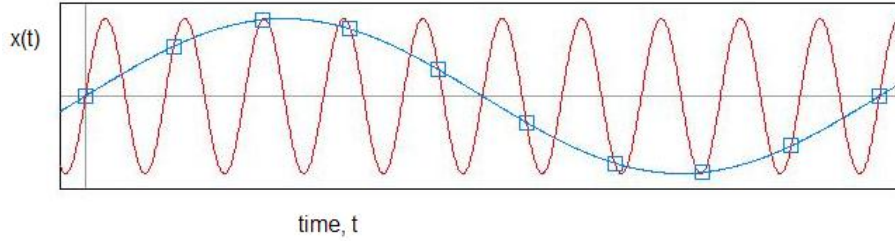


Figure 2.1: Diagram to illustrate the problems with the Nyquist frequency, from [6]

with the inverse discrete Fourier transform defined as,

$$f_j = \sum_{k=0}^{N-1} \tilde{f}_k e^{\frac{2\pi i j k}{N}},$$

where $j = 0, \dots, N - 1$, and k is the mode number. Here the DFT, \tilde{f}_k , is a complex number, its real part corresponds to the amplitude of the cosine waves and the imaginary part relates to the sine wave amplitude.

If we wish to sample a continuous signal using a sample interval, Δ and we define, from [14] and [6], the maximum frequency we are able to resolve using this interval as f_N , above which an unambiguous reconstruction of the signal is not possible then the frequency,

$$\frac{1}{2\Delta} = f_N,$$

is known as the *Nyquist frequency*.

Therefore, if 'N' data points are used in our Fourier transform, the highest mode number that can be resolved is $k = \frac{N}{2}$.

Figure 2.1 shows how sampling above the Nyquist frequency can confuse and create erroneous results. The blue curve shows the data being sampled within the Nyquist frequency, i.e. $|f| < \frac{1}{2\Delta}$. However, when the same sampling rate is used on a data set of much higher frequency (black curve), such

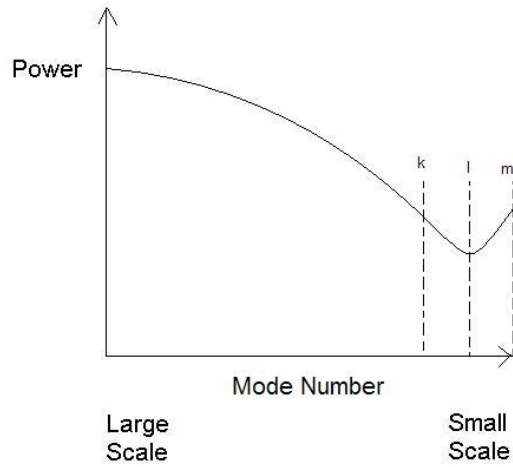


Figure 2.2: Diagram showing the folding of power between mode numbers k and l to between mode numbers l and m , adapted from [6]

that $|f| > \frac{1}{2\Delta}$, it would be impossible to distinguish between the two data sets using just the sampled points.

If a high frequency physical signal is not discretised frequently enough in order to resolve it correctly, the frequency function *folds* or *overlaps* on itself, in a process called *aliasing*, thereby forming an incorrect Fourier transform.

Figure 2.2 shows a simple example of what the aliasing effect, i.e. sampling a data set above the Nyquist frequency, would have on the power spectrum of a data set. As can be seen, there is a smooth decline in the power from large scales (low mode number). However as we reach the smallest scales, the power 'kicks' back up again. This is due to the aliasing effect on the data and is not accurate. In this example we can see that the power in between mode numbers k and l are folded over into the mode number range l to m .

For large values of N , the discrete Fourier transform (DFT) becomes computationally expensive, with the number of operations required to perform

the calculation approximately N^2 . In order to reduce the expense of the DFT, we may use a method called the *Fast Fourier Transform* (FFT) which reduces the number of operations to $O(N \log_2(N))$, [1].

When transforming a 2D set of $N \times M$ data into Fourier space we must use the corresponding 2D discrete Fourier transform, which is described from [6] as

$$\tilde{f}_{k,l} = \frac{1}{NM} \sum_{h=0}^{N-1} \sum_{j=0}^{M-1} f_{h,j} e^{-2\pi i(hk/N + jl/M)}, \quad (2.4)$$

for the discrete function, $f_{h,j}$, $h, k = 0, \dots, N-1$ and $j, l = 0, \dots, M-1$. Here k and l are defined as the mode numbers.

2.2 The Power Spectrum

The complex modulus of the DFT coefficients can be taken and then appropriately scaled in order to generate a plot which can be used to approximate the 'power spectrum' which gives the power associated with each wave mode present in the discrete set. These mode numbers correspond to different physical scales present in the discrete sample data, [5].

From Parseval's theorem, [1], we can show that the relation between the discrete Fourier transform and its inverse is as follows,

$$\frac{1}{N} \sum_{j=0}^{N-1} |f_j|^2 = \sum_{k=0}^{N-1} |\tilde{f}_k|^2, \quad (2.5)$$

which in 2D generalises to,

$$\frac{1}{NM} \sum_{h=0}^{N-1} \sum_{l=0}^{M-1} |f_{h,l}|^2 = \sum_{j=0}^{N-1} \sum_{k=0}^{M-1} |\tilde{f}_{j,k}|^2. \quad (2.6)$$

If we consider a function in one dimension, such that $f_j = \sin(\frac{2a\pi j}{N})$, with $a = 1, 2, 5, 7$ and $N = 32$, then calculate the power in this function from

(2.3), and using the fact that $|e^{-\frac{2\pi ijk}{N}}|^2 = 1$,

$$\sum_{j=0}^{N-1} \left| \sin\left(\frac{2a\pi j}{N}\right) \right|^2 = \frac{N}{2}$$

Then from Parseval's theorem, (2.5),

$$\sum_{k=0}^{N-1} |\tilde{f}_k|^2 = \left(\frac{N}{2}\right) / N = 0.5$$

Therefore, in order for the power spectrum to have an amplitude of 1, rather than 0.5, thereby making the power spectra easily comparable, we introduce a scaling factor of 4. Figure 2.3 shows the power spectrum of the function $f_j = \sin\left(\frac{2a\pi j}{N}\right)$ with $a = 1, 2, 5, 7$ and $N = 32$.

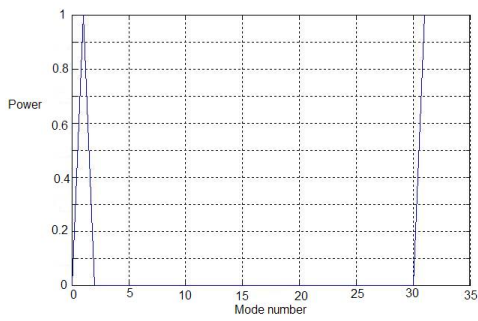
The power spectrum of the sine function produces two distinct peaks of equal amplitude. The location and periodicity of these peaks can be found in the following way, [5].

When the DFT is applied to a real sequence, f_j with $j = 0, \dots, N - 1$, the resultant will be, in general, a sequence of N complex numbers such that \tilde{f}_k and \tilde{f}_{N-k} are related, from [5], by

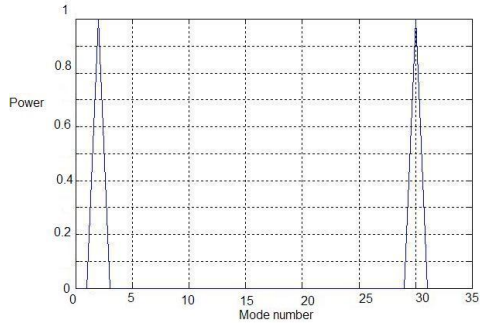
$$\tilde{f}_{N-k} = \tilde{f}_k^*$$

for $k = 0, \dots, N - 1$, where $*$ denotes the complex conjugate. This relation causes a periodic function to display the two distinct transform peaks, as seen in Figure 2.3. It also explains why we are seeing results in mode numbers corresponding to frequencies higher than the Nyquist frequency. The highest accessible mode number, corresponding to the Nyquist frequency, is $\frac{N}{2} = 16$. The power series does not supply us with any new information past the Nyquist frequency, the results are simply reflected [5].

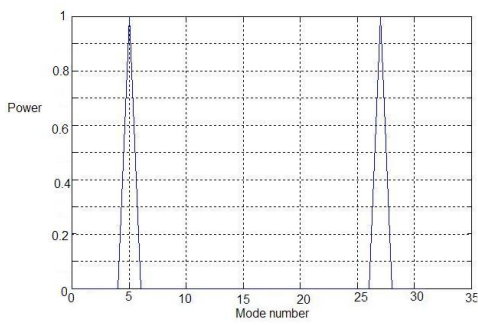
The position of the two peaks correspond to peaks of $\sin\left(\frac{2\pi aj}{N}\right)$ and



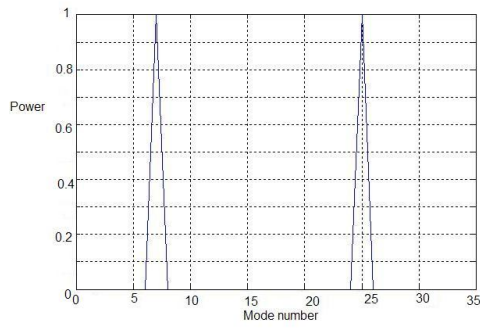
(a) Power spectrum of $\sin(\frac{2\pi j}{N})$



(b) Power spectrum of $\sin(\frac{4\pi j}{N})$

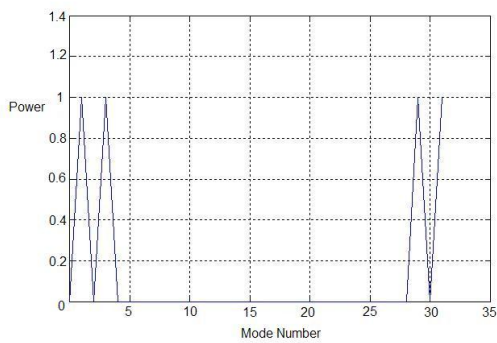


(c) Power spectrum of $\sin(\frac{10\pi j}{N})$

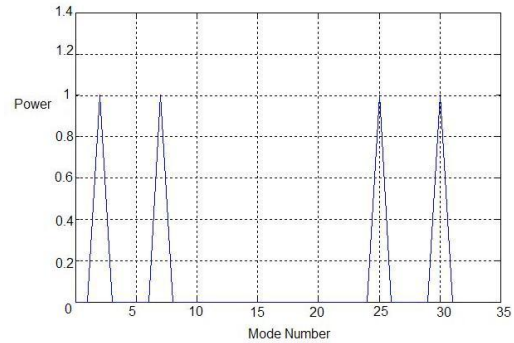


(d) Power spectrum of $\sin(\frac{14\pi j}{N})$

Figure 2.3: Power spectra for various sine functions



(a) Power spectrum of $\sin(\frac{2\pi j}{N}) + \sin(\frac{6\pi j}{N})$



(b) Power spectrum of $\sin(\frac{4\pi j}{N}) + \sin(\frac{14\pi j}{N})$

Figure 2.4: Power spectra for multiple sine functions

$\sin(\frac{2\pi a(N-j)}{N})$, so it can be seen that they appear at mode numbers a and $N - a$.

It is possible to use the power spectrum as an indicator of the wave pattern associated with a function. If we study the power spectrum of a function containing multiple waves, for example, $\sin(\frac{2\pi j}{N}) + \sin(\frac{6\pi j}{N})$ or $\sin(\frac{4\pi j}{N}) + \sin(\frac{14\pi j}{N})$ as shown in Figure 2.4, we can see that there is a peak in the power spectrum associated with each corresponding wavelength. Due to the Nyquist frequency, this will be the case for all mode numbers, $k < \frac{N}{2}$, since this is the largest mode number (corresponding to the smallest wavelength) representable on a grid with N points, [5].

Figures 2.3 and 2.4 show that the amplitude of the power spectrum remains constant as the mode number is varied. In Figure 2.5 we have introduced a scaling factor to the sine function, $\alpha \sin(\frac{2\pi j}{N})$, where α is a positive, real constant. Where the sine function has been scaled by a factor of α , the corresponding power spectrum has been scaled by a factor of α^2 . This corresponds to the squaring of the FFT, required to plot the power spectrum, meaning that we are now able to determine any scaling factors involved in the solution from the power spectrum, [5].

In order to obtain a discrete sequence of data from the continuous functions, used in this section, we looked at the coefficients of the Fourier series, which describe the continuous function under certain conditions, [5]. If, however, we are required to observe the power spectrum of a discrete set of data we must use a *periodogram*. The periodogram is a measure of the power based on discrete data and is analogous to approximating an integral by summing a series of boxes. The following section describes in detail the

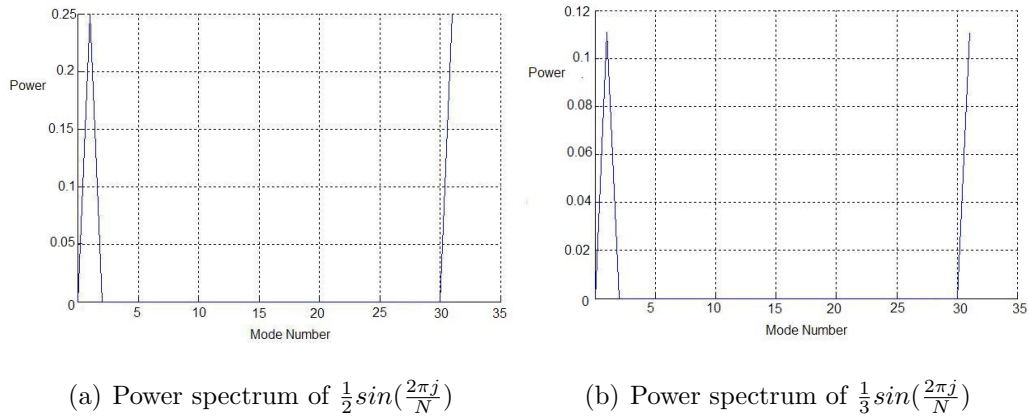


Figure 2.5: Power spectra for scaled sine functions

ideas behind the periodogram.

2.3 The Periodogram

As we have discussed in the previous section, the power spectrum of a function, f_j , may be estimated by taking the modulus squared of the discrete Fourier transform of some finite, sampled stretch of it, [5]. The power spectrum has been made easily comparable in the previous section by the inclusion of the normalisation factor, 4. In general, the measure of the squared amplitude of the function is proportional to the measure of the amplitude of the power spectrum. There are several different conventions for describing this relationship between the two spatial domains, for example, from [12],

$$\sum_{j=0}^{N-1} |f_j|^2 \equiv \text{sum squared amplitude}$$

$$\frac{1}{N} \sum_{j=0}^N |f_j|^2 \approx \frac{1}{T} \int_0^T |f(t)|^2 dt \equiv \text{mean squared amplitude}$$

$$\Delta \sum_{j=0}^N |f_j|^2 \approx \int_0^T |f(t)|^2 dt \equiv \text{time-integral squared amplitude,}$$

where T is the total sampling time, i.e. $T = N\Delta$, with Δ being the interval and N the total number of points sampled. The triangular rule is then applied in order to remove the final sampled point. In other words, we use $N + 1$ points to discretise the integral but only N points to define the periodogram.

There are even more possible ways in which to calculate the power spectrum, all of which have the characteristic of never integrating the spectrum outside the Nyquist interval, i.e. the sampling rate is below the Nyquist frequency. According to sampling theory, any power lying outside of this interval will be folded back into the region below the Nyquist frequency, [12].

One method used in estimating the power spectrum of a sampled function, is called a *periodogram*. If we apply an (N) -point fast Fourier transform to a discrete function, f_j to calculate its discrete Fourier transform,

$$\frac{1}{N} F_k = \sum_{j=0}^{N-1} f_j e^{-2\pi i j k / N} \quad k = 1, \dots, N - 1,$$

the periodogram used to estimate the power series of this discrete Fourier transform is defined at $\frac{N}{2} + 1$ frequencies as,

$$P(f_k) = [|F_k|^2 + |F_{N-k}|^2] \quad k = 1, 2, \dots, (\frac{N}{2} - 1)$$

$$P(f_c) = P(f_{N/2}) = |F_{N/2}|^2$$

where f_c is the Nyquist frequency, f_k is defined for zero and positive frequencies and $P(f)$ denotes the power spectrum calculated. From (2.5) it can be shown that the definition of the periodogram is normalised so that the sum

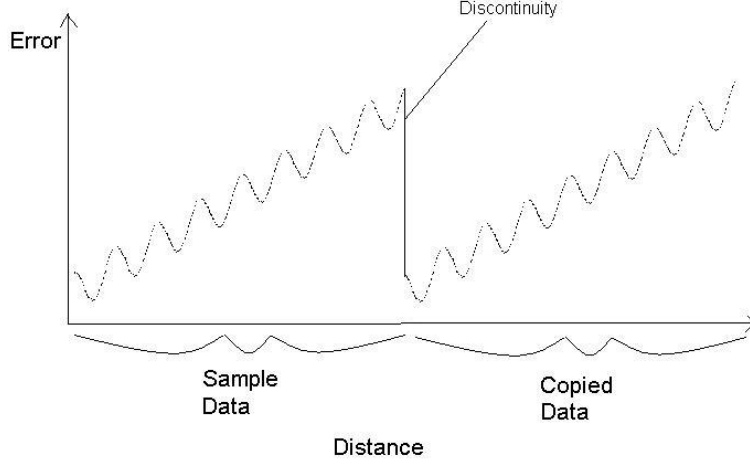


Figure 2.6: Diagram showing a discontinuity forming due to the FFT

of the periodogram is equal to the variance of the function. Notice that the estimate of the power spectrum at each frequency, f_k , can be thought of as

$$\frac{f_{k-\frac{1}{2}} + f_{k+\frac{1}{2}}}{2}.$$

In two dimensions, we define the periodogram at $(\frac{n}{2} - 1 \times \frac{m-1}{2})$ frequencies as, [8],

$$\begin{aligned} P(f_{j,k}) &= 2[|F_{j,k}|^2 + |F_{n-j,k}|^2] & j = 1, \dots, \frac{n}{2} - 1, k = 1, \dots, \frac{m-1}{2} \\ P(f_{\frac{n}{2},k}) &= 2|F_{\frac{n}{2},k}|^2, & k = 1, \dots, \frac{m-1}{2} \\ P(f_{j,0}) &= 2|F_{j,0}|^2, & j = 1, \dots, \frac{n}{2} - 1 \\ P(f_{0,k}) &= 2|F_{0,k}|^2, & k = 1, \dots, \frac{m-1}{2} \\ P(f_{\frac{n}{2},0}) &= |F_{\frac{n}{2},0}|^2. \end{aligned} \tag{2.7}$$

If we wish to create a periodogram of non-periodic sample data, we may encounter problems and indeed anomalies within the power spectrum. These are created when the fast Fourier transform copies the sampled data and

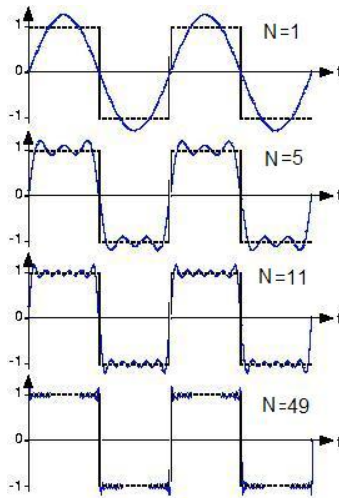


Figure 2.7: Fourier series approximation to a square wave discontinuity, using number of sampling points, $N = 1, 5, 11, 49$, [4]

adds it to the end in order to create false periodicity, as shown in Figure 2.6. Where the copy and the original data of a non-periodic sample meet, a discontinuity may form. This is due to the value at the end of the original data having a different value to the beginning, so where it meets the copy, the two ends do not meet. Now, when the fast Fourier transform tries to transform this discontinuity into Fourier space, high frequency waves are created along it. Figure 2.6 shows a discontinuity forming, as a set of sample data is copied in order to create false periodicity.

These waves have a higher frequency than that of the Nyquist value and so aliasing occurs, thereby increasing the power to the high frequency region of the periodogram. This process was first explained by J. Willard Gibbs in 1899, and therefore these discontinuous points are referred to as *Gibbs phenomenon*.

nomena, [2].

The Gibbs' phenomena is illustrated in Figure 2.7 by showing how a Fourier series approximates a square wave discontinuity. We can see that the fewer sampling points used by the Fourier series, the worse the approximation is. This same effect occurs on the discontinuity shown in Figure 2.6, and leads to aliasing effects shown in Figure 2.2.

One possible method and indeed the method used in this project, for reducing the Gibbs' phenomena from a set of non-periodic sample data is known as *detrending*. The most commonly used technique for detrending data is to fit a first order polynomial, or at least a low order one, to the data, then subtract it from the sample. This has the effect of reducing the distance in height between the two end points, so that the discontinuity created when the Fourier transform creates a false periodicity is reduced. The effect of this is to reduce the aliased power in the high frequency range of the periodogram.

Detrending also effects the low frequency end of the spectrum, which can no longer be regarded as reliable. This is not a major problem as the trends cannot be described by the lowest frequency therefore removing them does not change the overall result.

When forming the power spectrum of a two dimensional sample of data, we need to use a plane surface to detrend the data, [2].

In Figure 2.8 we show the detrending method used to reduce Gibbs' phenomena. As shown in the diagram, we begin with a set of data then remove its trend. In doing so we re-align the data set about zero and when we now use this set as in Figure 2.6, to transform it into Fourier space, we reduce the likelihood of creating a large discontinuity between the data and its copy.

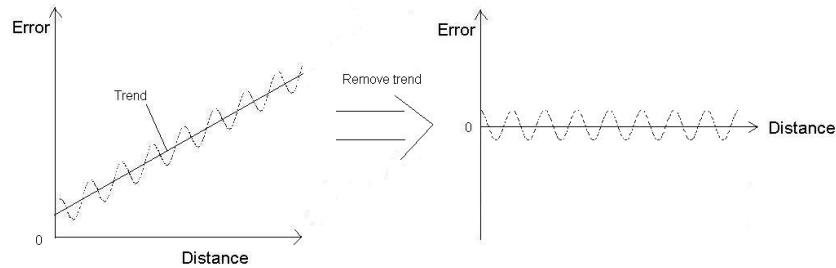


Figure 2.8: Diagram showing detrending of a sample data set

We recall that in order to use the FFT on a discrete set of data, the FFT assumes periodicity in the data and so copies the data and adds it to the end of the domain. In order to reduce the sample domain to the original size, the data set is multiplied by a rectangular domain, which is equal to 1 over the domain of the data and zero everywhere else, as shown in Figure 2.9.

These domain truncations can cause unacceptable approximations to the Fourier transform, [6]. In the case where we use a discrete set of non-periodic data, we must employ data windowing in order to produce a better estimate of the Fourier transform. This is discussed in the next section.

2.4 Data Windowing

As previously discussed in section 2.3, while looking at non-periodic discrete data, we may employ windowing techniques in order to reduce the undesired effects of domain truncation by the rectangular window.

The basic idea behind data windowing is to massage the sample data in order to approximate the power spectrum by the periodogram more closely.

The multiplication of a discrete data set by a rectangular window function,

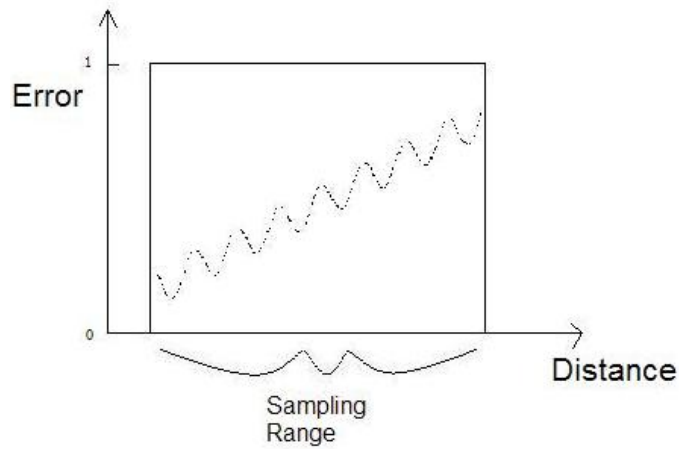


Figure 2.9: Diagram showing the square window multiplied by the sample data

creates discontinuities at the edges of the domain. When these discontinuities are resolved by the FFT, Gibbs' phenomena occur, causing false high frequency oscillations in the results. This effect is called *leakage*, [12].

Figure 2.9 shows a rectangular spatial window being applied to a set of data. As can be seen, at the edges of the domain, the data suddenly changes from a non-zero to a zero value, thereby causing a discontinuity to form.

We now define the data window function, w_j , applied to the domain $[0, N]$, as

$$\begin{aligned} w_j &= 1, \quad j = 0, \dots, N \\ &= 0, \quad \text{everywhere else.} \end{aligned}$$

Now we define W_{ss} as the window squared and summed,

$$W_{ss} = \sum_{j=0}^N (w_j)^2$$

In order to account for the data set being multiplied by this window function, when we calculate the periodogram the normalisation factor, $\frac{N}{W_{ss}}$, must also be introduced.

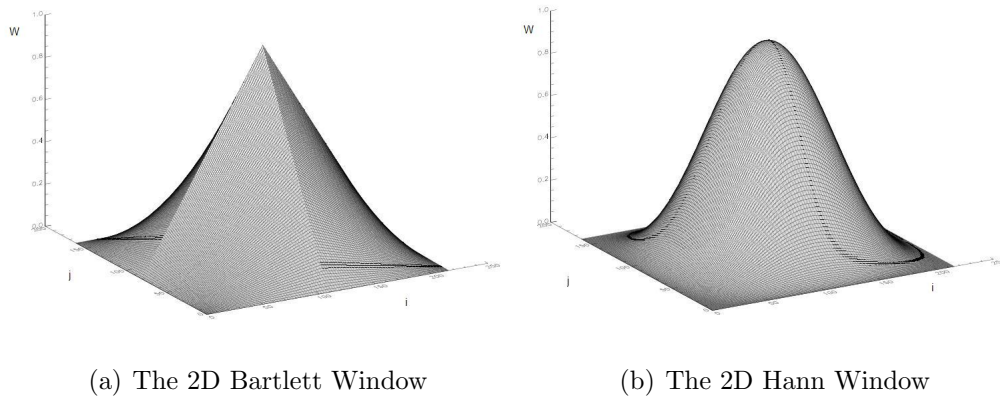


Figure 2.10: 2D windowing function

The technique of data windowing looks to modify the function, w_j , so that discontinuities no longer form at the edges of the spatial domain.

There are many variations of the window function, all of which involve starting at zero at the domain edges and gradually increasing to a maximum value of 1 at the middle of the domain. Two of the more popular window functions are the Bartlett and Hann windows, [12], described in 1D as,

$$w_j = 1 - \left| \frac{j - \frac{1}{2}N}{\frac{1}{2}N} \right| \equiv \text{"Bartlett Window"},$$

$$w_j = \left[1 - \cos \left(\frac{\pi j}{N} \right)^2 \right] \equiv \text{"Hann Window"}.$$

The Bartlett window produces slopes of constant gradient which lead to the maximum, conversely the Hann window has smooth slopes, with increasing gradient, due to the cosine function used. The summit of the Hann window is smooth and rounded, as opposed to the sharp peak of the Bartlett window. As part of this project the data fields being examined will be in 2-dimensions and we therefore need to define these window functions for a 2D region of

size $(M \times N)$ with N even and M odd:

$$w_{i,j} = \left(1 - \left|\frac{2i}{N} - 1\right|\right) \left(1 - \left|\frac{2j}{(M-1)} - 1\right|\right) \equiv \text{"2D Bartlett Window"}, \quad (2.8)$$

$$w_{i,j} = \left(1 - \cos(\pi i/N)\right)^2 \left(1 - \cos(\pi j/M)\right)^2 \equiv \text{"2D Hann Window"}. \quad (2.9)$$

These window functions are displayed in Figure 2.10. As can be seen, the window function starts at zero and gradually increases to a maximum value of 1 and then returns back to zero.

The corresponding normalising factor for the 2D periodogram is now

$$\frac{NM}{\sum_{i=0}^N \sum_{j=0}^M (w_{i,j})^2}.$$

The next Chapter looks at the full and incremental 4D-Var assimilation methods in detail. It is the incremental version which we shall be using in this project to study the evolution of the scales present in the forecast error.

Chapter 3

The Model and Methodology

In Chapter 3 we discuss the full 4D-Var data assimilation method and the incremental 4D-Var assimilation method. We shall use the incremental method in this project as it is this method which is used by the UK Met Office in numerical weather prediction.

We look at the full 4D-Var method because one of the few pieces of work on the evolution of forecast errors was done using this method on a simplified model. We shall be looking at the incremental method on the UK Met Office numerical weather prediction model, which has not previously been studied.

3.1 Full 4D-Var Assimilation

The data assimilation process aims to incorporate observed measurements into a dynamical system model in order to produce accurate estimates of all the state variables over a period of time, known as the assimilation window, [11]. We aim to minimise the square errors between the model predictions and the observed system states. In other words 4D-Var data assimilation

aims to find the model state, \mathbf{x}_0 , which minimises the cost function, in the time window $[t_0, t_n]$

$$\mathcal{J}[\mathbf{x}_0] = \frac{1}{2}(\mathbf{x}_0 - \mathbf{x}^b)^T \mathbf{B}_0^{-1}(\mathbf{x}_0 - \mathbf{x}^b) + \frac{1}{2} \sum_{j=0}^n (H_j[\mathbf{x}_j] - \mathbf{y}_j^0)^T \mathbf{R}_j^{-1} (H_j[\mathbf{x}_j] - \mathbf{y}_j^0), \quad (3.1)$$

subject to the discrete nonlinear model

$$\mathbf{x}_j = S(t_j, t_0, \mathbf{x}_0).$$

Here \mathbf{x}^b is a background field, \mathbf{y}_j^0 are the observations, H_j is the observation operator used to map the fields from model space onto observational space and $S(t_j, t_0, \mathbf{x}_0)$ is the solution operator of the nonlinear model. The background and observational errors are stored in the covariance matrices, \mathbf{B}_0 and \mathbf{R}_j respectively, [10].

The idea behind the full 4D-Var assimilation method is to solve the full nonlinear cost function using an iterative process where k is the iteration number, [3],

1. Set $\mathbf{x}_0^{(k)} = \mathbf{x}^b$, where $k = 0$ and \mathbf{x}^b is the background field.
2. Run the nonlinear model and calculate the cost function, $\mathcal{J}(\mathbf{x}_0^{(k)})$.
3. Find the gradient of the cost function, $\nabla \mathcal{J}(\mathbf{x}_0^{(k)})$, using the adjoint method.
4. Using results from steps 2 and 3 update $\mathbf{x}_0^{(k)}$.
5. Go back to step 2.

This process uses an iterative method such as quasi-Newton or conjugate gradient to solve it and is continued until, either an appropriate number of

steps had been taken, or the solution had converged sufficiently.

Previous work by Tanguay et al., [15], has looked at how the error between the analysis field created by the assimilation process and the initial background field (known as the forecast error) evolves over one iteration of this process, and is discussed in chapter 4.

3.2 Incremental 4D-Var Assimilation

As in the full 4D-Var assimilation method, we define the incremental method as finding the model state, \mathbf{x}_0 , which minimises the cost function (3.1). This minimisation procedure can carry extremely high computational cost due to the nonlinear nature of the observation operator and numerical model as before, which cause the cost function, \mathcal{J} , to be a nonlinear least squares problem, [10].

The reduction in computational cost is achieved by approximating the full problem by a series of minimisations of approximate quadratic cost functions. We can view the 4D-Var process as the following iterative procedure, [10], where k is the iteration number:

1. We begin by defining a guess field, $\mathbf{x}_0^{(k)}$. For $k = 0$, the first iteration, we set the background field, \mathbf{x}^b , equal to the guess field, $\mathbf{x}_0^{(0)}$.
2. We run the nonlinear model in order to calculate the field states, $\mathbf{x}_j^{(k)}$, at each time step t_j .
3. For each observation, \mathbf{y}_j^0 , we calculate the innovation vectors $\mathbf{d}_j^{(k)} = \mathbf{y}_j^0 - H_j[\mathbf{x}_j^{(k)}]$.

4. An incremental field is then defined as $\delta \mathbf{x}_0^{(k)} = \mathbf{x}_0^{(k+1)} - \mathbf{x}_0^{(k)}$.
5. The value of $\delta \mathbf{x}_0^{(k)}$ is found, which minimises the cost function,

$$\begin{aligned} \tilde{\mathcal{J}}^{(k)}[\delta \mathbf{x}_0^{(k)}] &= \frac{1}{2}(\delta \mathbf{x}_0^{(k)} - [\mathbf{x}^b - \mathbf{x}_0^{(k)}])^T \mathbf{B}_0^{-1}(\delta \mathbf{x}_0^{(k)} - [\mathbf{x}^b - \mathbf{x}_0^{(k)}]) \\ &\quad + \frac{1}{2} \sum_{j=0}^n (\mathbf{H}_j \delta \mathbf{x}_j^{(k)} - \mathbf{d}_j^{(k)})^T \mathbf{R}_j^{-1}(\mathbf{H}_j \delta \mathbf{x}_j^{(k)} - \mathbf{d}_j^{(k)}). \end{aligned} \quad (3.2)$$

subject to

$$\delta \mathbf{x}_j^{(k)} = \tilde{\mathbf{L}}(t_j, t_0, \mathbf{x}^{(k)}) \delta \mathbf{x}_0^{(k)}$$

where \mathbf{H}_j is the linearisation of the observational operator H_j around the state $\mathbf{x}_j^{(k)}$ and $\tilde{\mathbf{L}}(t_j, t_0, \mathbf{x}^{(k)})$ is the solution operator of the linear model linearised around the nonlinear model trajectory.

6. We update the guess field using,

$$\mathbf{x}_0^{(k+1)} = \mathbf{x}_0^{(k)} + \delta \mathbf{x}_0^{(k)}.$$

7. The procedure is repeated until a convergence threshold has been reached or after a set number of iterations has passed. We can now define an analysis field as the updated guess field, i.e. $\mathbf{x}^a = \mathbf{x}^{(M)}$, where M is the number of iterations performed.

Each iteration of this procedure is known as an *outer loop* and with each outer loop, the minimisation of the cost function (3.2) must be solved in another iterative procedure known as an *inner loop*, [10]. The solving of each inner loop may be thought of as a convex quadratic minimisation problem and as a consequence can be solved using methods such as the *quasi-Newton method* or the *conjugate gradient method*, [10].

It is possible to think of the incremental field, after it has converged sufficiently, as the difference between the background guess and the converged analysis field, i.e. the error between our initial guess and the analysis we have converged to,

$$\sum_{k=0}^M \delta \mathbf{x}^{(k)} = \mathbf{x}^a - \mathbf{x}^b. \quad (3.3)$$

where M is the total number of iterations of the inner loop.

There has been little work on how the error, between the analysis and background field states, evolves as the number of iterations in the inner loop increase. Moreover, this work has only been conducted using simple models, such as the *barotropic vorticity equation*. In section 4 we discuss past work on this analysis of forecast errors.

Chapter 4

Previous Work on Forecast Error

As part of this chapter we discuss previous work on the evolution of the error between the analysis field and the initial background field through the full and incremental 4D-Var assimilation process.

All previous work has only been done using the simple barotropic vorticity equation model, whereas we shall be studying the nonlinear numerical weather prediction model used at the UK Met Office, which has never been used to investigate this question.

4.1 Four-dimensional Data Assimilation with a Wide Range of Scales

The paper written by Tanguay, Bartello and Gauthier entitled ‘Four-dimensional data assimilation with a wide range of scales’ looks at

whether it is possible for the adjoint method, used in the full 4D-Var process, to improve initial conditions in data-sparse regions of observational field data. They examine the method's ability to 'fill in' small scale detail determined dynamically from large scale data, [15].

The numerical model chosen for this piece of work was the barotropic β -plane flow, due to its simple geophysical settings and the wide range of scales involved. The barotropic vorticity equation on the β -plane approximation is defined as

$$\frac{\partial \zeta}{\partial t} + \mathbf{J}(\Psi, \zeta) + \beta v = f - \mathcal{D}(\zeta), \quad (4.1)$$

where $\Psi = -U_0 y + \psi$, U_0 is the mean zonal wind (with dimensionless units) taken to be 0.3, y is the distance in the north-south direction, ψ is the stream function, $\zeta = \nabla^2 \psi$, (the relative vorticity), $u = -\partial \psi / \partial y$, (the wind field in the east-west direction), $v = \partial \psi / \partial x$, (the wind field in the north-south direction), \mathbf{J} is the Jacobian, f is a forcing term, β is the coriolis parameter and \mathcal{D} is a linear dissipation operator, [15].

The tangent linear model was introduced as an intermediate step in order to derive the adjoint model of the problem. This was done by considering a reference solution to the nonlinear equation, ζ and a perturbation about that solution, $\delta \zeta$. Then writing (4.1) for the total field $\zeta + \delta \zeta$ and then subtracting the equation for ζ to get, [15],

$$\left[\frac{\partial}{\partial t} + U_0 \frac{\partial}{\partial x} \right] \delta \zeta + \mathbf{J}(\psi, \delta \zeta) + \mathbf{J}(\delta \psi, \zeta) + \mathbf{J}(\delta \psi, \delta \zeta) + \beta \delta v = -\mathcal{D}(\delta \zeta). \quad (4.2)$$

This becomes the *tangent linear model* by neglecting the term, $\mathbf{J}(\delta \psi, \delta \zeta)$.

In one of the experiments undertaken by Tanguay et al. (1994) while investigating the adjoint method's ability to fill in small scale detail from larger scales, they looked at the convergence of the forecast error using the full 4D-

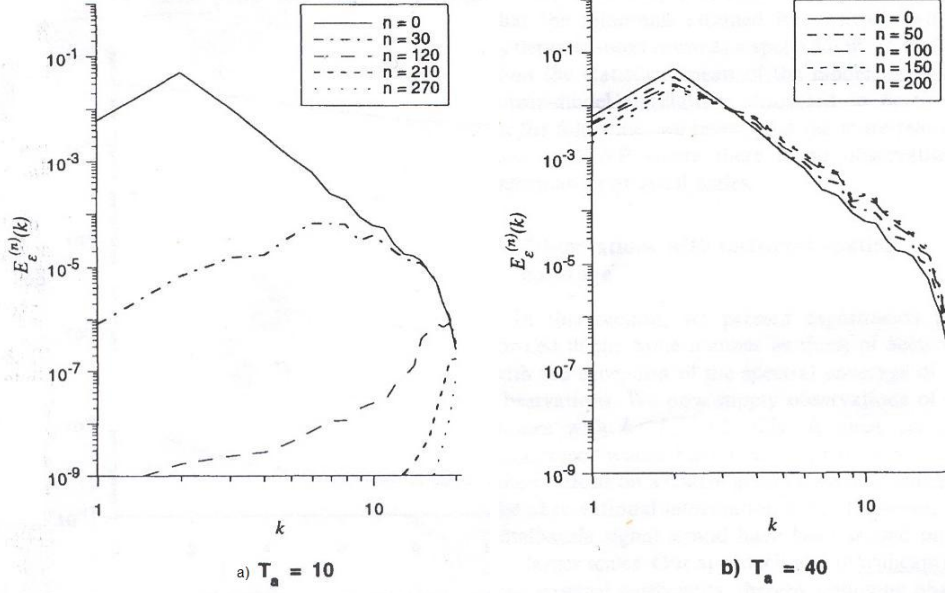


Figure 4.1: Evolution of forecast error through the adjoint method of the full 4D-Var process, using assimilation window of size a) $T_a = 10$ and b) $T_a = 40$

Var method applied to (4.2). The error field was defined as $\epsilon^{(n)} = \zeta^{(t)} - \zeta^{(n)}$, where $\zeta^{(t)}$ is the true analysis field of relative vorticity created from by an integration of the nonlinear model, $\zeta^{(0)}$ is the initial background estimate field and $\zeta^{(n)}$ is the relative vorticity at the n th iteration of the adjoint method, [15]. Using one iteration of the full 4D-Var outer loop, they observed how the difference between the true analysis field and the updated background field, converge through the iterative adjoint method, described in section 3.1.

Figure 4.1 shows the results taken from [15], showing the evolution of the forecast error over the process of the adjoint method, using one outer loop and two different assimilation periods. The graphs show wave number plotted against power in the forecast error and the various curves represent the different iteration numbers, n .

The assimilation window is defined as the period of time over which the assimilation process takes place. Figure 4.1(a) uses an assimilation window of size $T_a = 10$ model time units (≈ 3 days). Tanguay et al. concluded that the results in figure 4.1(a) showed that right from the start of the assimilation process, the adjoint method converged and the largest scales were adjusted to fit the observations. As the iterations proceeded, the minimisation focused its attention on increasingly smaller scales until, after about two hundred iterations, virtually all of the error was in the smallest scales,[15]. It can be seen that after a very short time, almost all of the error disappears. Tanguay et al., [15] concluded that since the errors at $t = 0$ (the initial time) are confined to the smallest scales, the initial small-scale field is only weakly dynamically coupled to the rest of the observational data, [15].

Figure 4.1(b) uses an assimilation window of size, $T_a = 40$ model time units (≈ 13 days). This was done in order to investigate the convergence when the assimilation period is long compared to the nonlinear timescale of the model. We see, in figure 4.1(b), that the convergence of the larger scales is very slow and more importantly the method appears to be diverging in the smaller scales. This shows that the consequence of having an assimilation period that exceeds beyond the validity time scale of the tangent linear model is that the solution at the end of the time period has essentially lost its memory of the initial conditions, which constitutes the limit of the method, [15].

The reason given in the paper for the divergence at smaller scales is the non-linearity of the problem causing the cost function, instead of being quadratic as assumed, forming a second minimum. Therefore, an incorrect value of the

model state, which minimises the cost function, may be chosen.

We will now discuss a paper which uses the same model but uses the incremental 4D-Var method instead of the full method.

4.2 A Validation of the Incremental Formulation of 4D Variational Data Assimilation in a Nonlinear Barotropic Flow

This paper, written by Laroche and Gauthier, [9], investigated the ability of the incremental approach to 4D-Var to reduce computational cost, in order to meet operational limitations of the full 4D-Var method.

As with the paper written by Tanguay et al. ,[15], the model used in this paper was the physically simple 2D barotropic vorticity equation on a β -plane approximation (4.1).

The results in [9] which are most pertinent to our work are those obtained without updating the outer loop trajectory. These examine the convergence properties of the incremental 4D-Var method, without updating the reference directory, i.e. when only one outer loop iteration is performed. As part of this experiment they compared the convergence of the incremental method with the convergence of a full low-resolution method (which acted as the control run), over a number of iterations of the inner loop at the beginning of the assimilation process.

In order to observe the convergence of these methods, Laroche and Gauthier studied the energy spectrum of an error field defined as the difference between the vorticity obtained after a given number of iterations and the

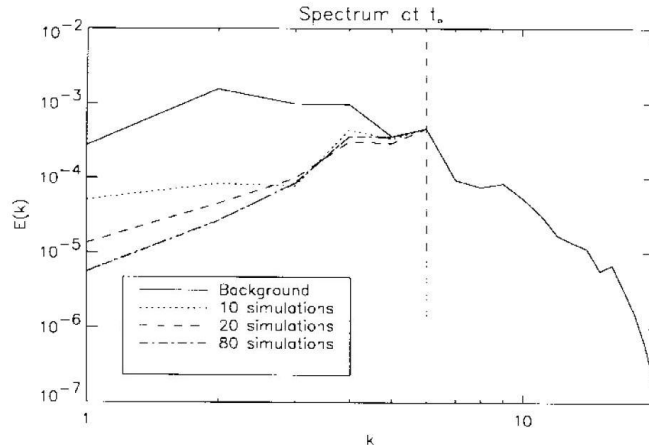


Figure 4.2: Error spectrum at time, t_0 for the incremental approach, [9], the vertical line indicates the mode number k_L

control run created from an integration of the nonlinear model.

In these experiments the models were not used to assimilate data with mode numbers greater than $k_L = 5$. This is because they believed this to be the best choice to enhance the interactions between the resolved and unresolved scales, [9]. Figure 4.2 shows how the error spectrum evolves and converges throughout the first eighty iterations of the inner loop for the incremental approach to the 4D-Var method. As with the work presented in [15], the error spectrum in the larger scales reduces right from the start, although not to the same extent as shown in figure 4.1(a). Then the smaller scales (ignoring mode numbers larger than k_L) begin to reduce in the first 20 iterations, but then after 80 iterations of the inner loop, the power in the smaller scales begins to increase as the solution diverges.

This same divergence phenomenon appears in [15] where the assimilation window is larger than the nonlinear validity timescale of the model.

Figure 4.3 shows the error spectrum for the first eighty iterations of the

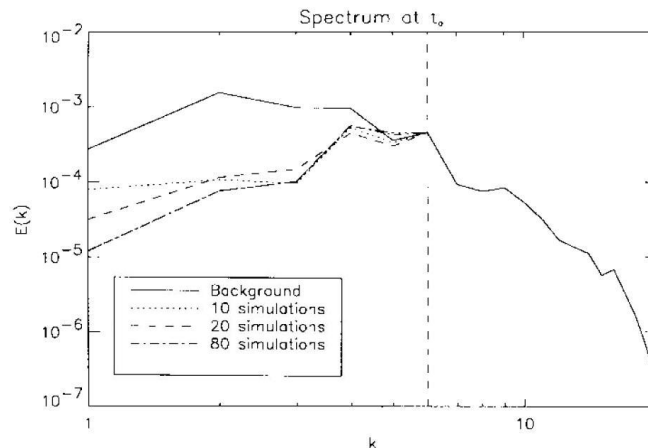


Figure 4.3: Error spectrum at time, t_0 , for the full low-resolution approach, [9]

inner loop, using the full low-resolution approach to 4D-Var assimilation.

Again, the larger scales reduce in power quickly, after only a few iterations and the smaller scales take more time to reduce in power. As with Figure 4.2 we see the solution diverging in the small scales, with it being even more pronounced when using the full low-resolution approach. After eighty iterations of the inner loop, the divergence is such that there is more power located in the smaller scales than there was in the initial background field.

In this project we intend to move forward from the pieces of work discussed in this section and investigate the evolution of the forecast error using the incremental 4D-Var method applied to the nonlinear numerical weather prediction model used at the UK Met Office. This project has never been done before and we therefore intend to compare the results of this investigation with those obtained by the pieces of work in this chapter.

The next chapter describes the numerical experiments we undertook to

obtain our results.

Chapter 5

Numerical Experiments

In this chapter we run the incremental 4D-Var process on the UK Met Office numerical weather prediction model outputting the forecast error every few iterations of the inner loop, in order to investigate the evolution of the scales present in the incremental data.

We describe, as we come to them, the steps taken and the thought processes involved in finding the best combination of accuracy and comparability between results to display the forecast error at each iteration.

5.1 2D Periodogram

We begin by running the incremental 4D-Var method, over one outer loop, (as described in section 3.2) on the Met Office numerical weather prediction model. The full operational observation data was used and we examined the incremental data on the full global scale (432x325 numerical grid points), at the surface level.

In order to investigate the best way to display the results, we began by

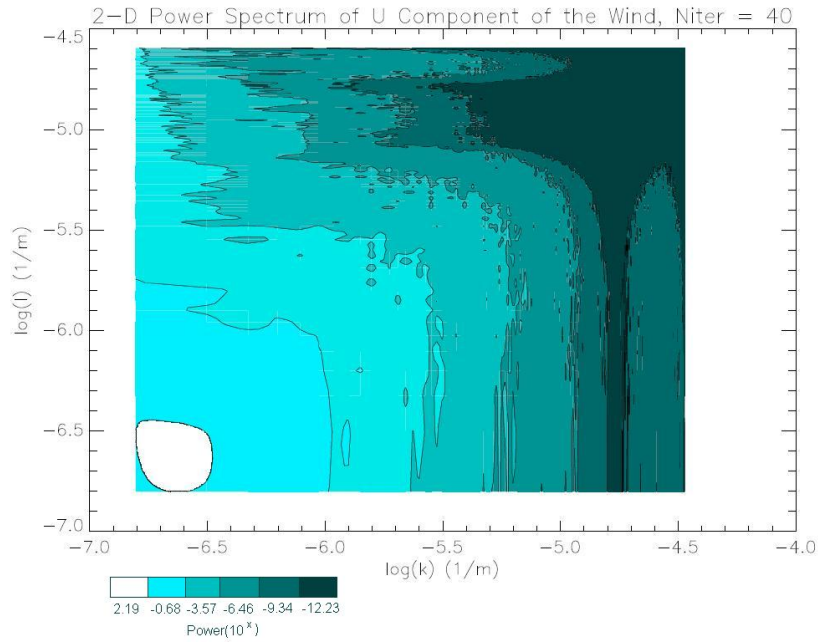


Figure 5.1: 2D periodogram of the incremental east-west component of the wind field, after 40 inner loop iterations.

analysing the incremental field data of the east-west component of the wind field at the surface, after the full 40 iterations of the inner loop.

This field data was then transformed into Fourier space using the 2D fast Fourier transform, (2.4) and using the 2D periodogram, (2.7), we were able to produce a measure of the power based on the DFT.

Figure 5.1 shows the 2D periodogram of the incremental east-west component of the wind field. The x and y axis display the logarithm of base 10 of the mode numbers in those directions. We display the power in terms of a contour plot, with the brighter colours representing higher powers.

It can be seen that in the bottom left corner we have an area of white (therefore high power), corresponding to a power of $10^{2.19}$. Since physical

scales are inversely proportional to the mode number and this area has the smallest mode numbers, it corresponds to the largest physical scales. As we move across the x-axis, note the decrease in power levels as the value of the mode number increases, this is entirely to be expected and is also shown in figure 4.1, from [15].

Moving further along the x-axis, towards the smaller scales, we note that the power level ‘kicks’ back up at the smallest scales, shown as the lobe of brighter colour in Figure 5.1. From section 2.1 we already know that this is indicative of aliasing due to frequencies higher than the Nyquist frequency being resolved by the FFT.

If the 2D periodogram is viewed in the x-z plane (where the z-axis represents the power scale, and is coming out of the plot), it can be seen that the power reduces from the largest scales to the smaller scales, then ‘kicks up’ in the smallest scale. This has been identified as an effect of aliasing, as shown in Figure 2.2 and described in section 2.1.

We believe the odd behaviour located along the top of the plot to be caused by the problems faced by the global model on the poles, which act as singularities, since on a rectangular grid the entire top row is defined in such a way as to represent one point (the north pole). We have periodicity around the globe but at the poles, in order to discretise the model, several points are chosen at the top and bottom of the region to have the same value. This allows us to ‘unfold’ the globe and display it on a rectangular grid.

In order to try and reduce the impact of aliasing on our results, we now introduce the detrending technique, described in section 2.3, to the incremental data. The PV-wave program, used at the UK Met Office, was used

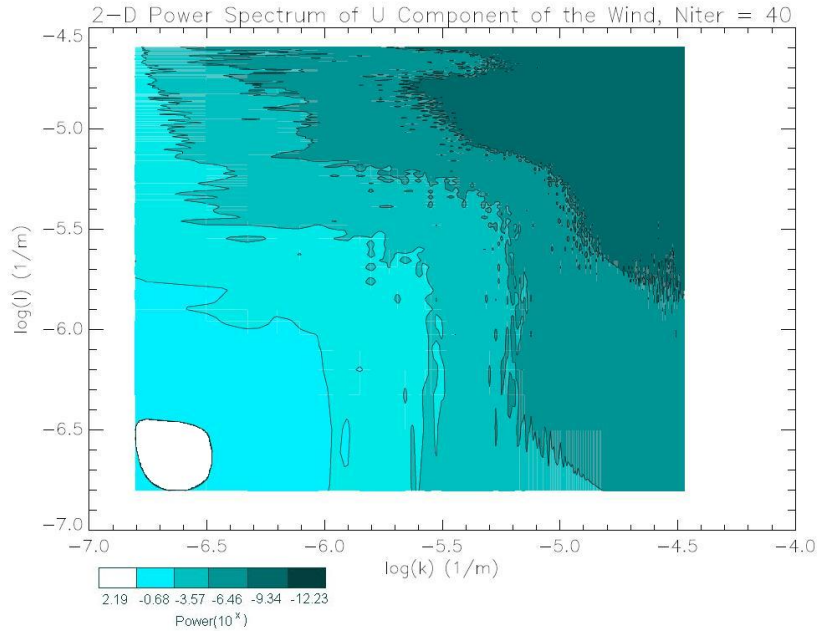


Figure 5.2: 2D periodogram of the incremental u-component of the wind field, after 40 inner loop iterations, using the detrending technique.

to look for a best fit plane to the original data set in physical space. This was then subtracted from the data and the FFT was taken again to transform the results into Fourier space and the 2D periodogram was formed. The detrended 2D periodogram is shown in figure 5.2.

The aliasing problem seems to have been dramatically reduced by the introduction of the detrending method. As can be seen, the highest power is located in the largest scales and as the mode number increases, corresponding to a decrease in the physical scales, the power also reduces. This was expected and is demonstrated in results by Tanguay et al. (Figure 4.1), [15], and by Laroche et al. (Figures 4.2 and 4.3), [9].

The same power scales were used in the production of both 2D peri-

odograms in order to improve comparability of results. It can be seen that after the detrending technique was used on the incremental data, the power in the smallest scales was increased from approximately $10^{-12.23}$ before the detrending to approximately $10^{-9.34}$ after detrending.

To investigate this alteration in the power at small scales we decided to plot the absolute value squared of the Fourier coefficients of the incremental data, against its corresponding mode number, on a full 1D power series scatter plot, described in the next section.

5.2 The full 1-D power series scatter plot

This section describes the investigation of the increase in power, in the 2D periodogram, located in the smallest scales, as a result of the application of the detrending technique to the incremental data.

This time, instead of looking at the east-west component of the wind field, we studied the surface pressure after one iteration of the inner loop. This is due to the understanding that the surface pressure is regarded as the most reliable state variable calculated by the UK Met Office model.

We began by looking at the results of incremental data before the detrending technique was applied. These results were transformed it into Fourier space by the FFT. We then calculated the absolute value squared of the Fourier coefficients and plotted them against their corresponding mode numbers. This left us with a full 1D power spectrum scatter plot containing different mode numbers with the same power and also different powers in the same mode number.

Figure 5.3 shows the scatter plot of the full power spectrum located at

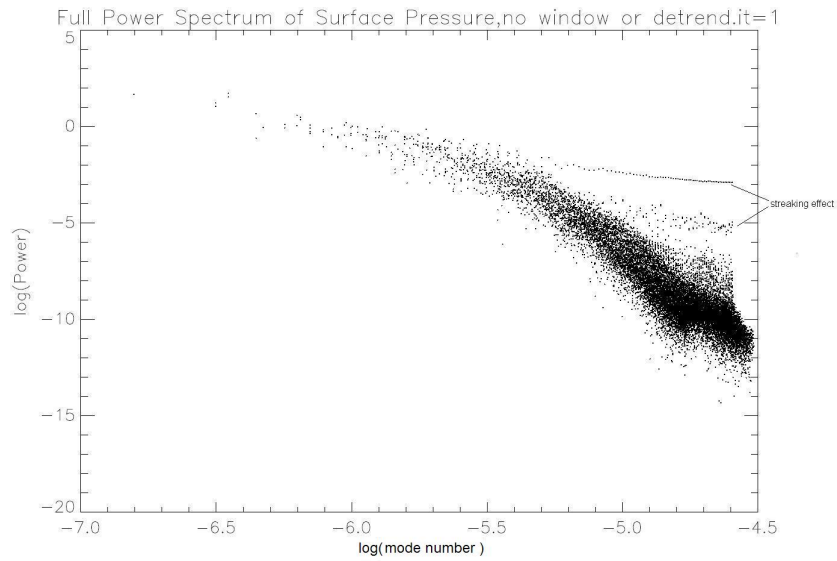


Figure 5.3: Full 1D power series scatter plot, after one inner loop iteration.

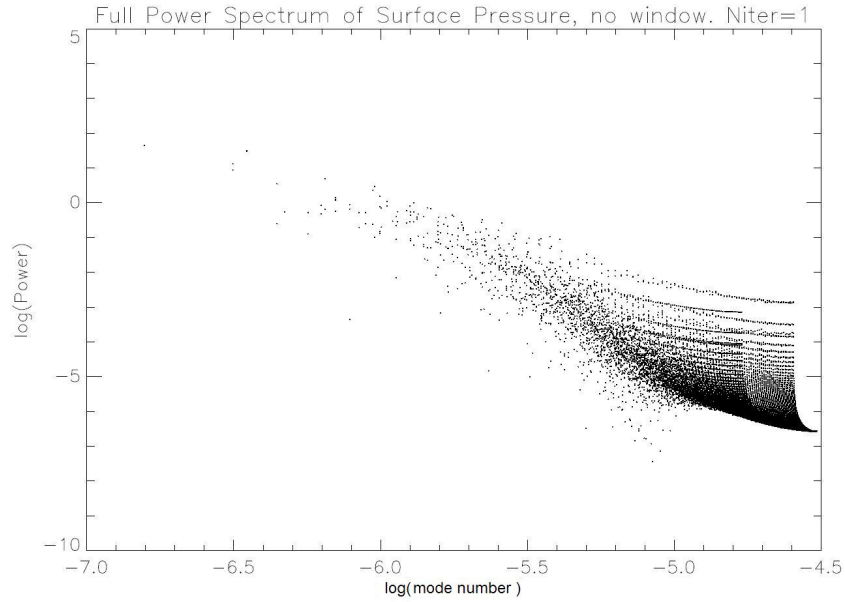


Figure 5.4: Full 1D power series scatter plot, after one inner loop iteration and using detrending.

each mode number for the surface pressure increment after one inner loop iteration, without the use of the detrending technique.

The idea of this plot was to help us to understand the increase in power in the small scale data when the detrending technique was applied to the 2D periodogram.

Before the detrending technique was applied the distribution of power appears to be as expected, with more points in the small scale region indicating a lot of noise in the original data. There also appears to be some sort of streaking effect occurring in the data, creating trails at higher powers than the general trend would indicate (indicated on the plot).

We now apply the detrending technique to the incremental data and display the full spectrum of the result. This is shown in figure 5.4.

Although the detrending technique removed the problem of aliasing in the 2D periodogram, it leaves us with a lot more streaking effects in the full power spectrum. We believe these streaks are the cause of the increase in power in the small scales found in the periodogram. After careful analysis of the raw data, it was discovered that these streaks corresponded with the data at the edges of the physical domain.

As discussed in section 2.4, the use of a rectangular window function on the data can cause unacceptable approximations to the Fourier transform. We believe these streaks to be an artifact of the truncation of the domain due to the rectangular window function, since the effect appears to be located in the data at the edges of the physical domain. We therefore decided to employ the windowing technique in order to control this streaking. The two physical window functions, in 2D, used were the Hann and Bartlett windows

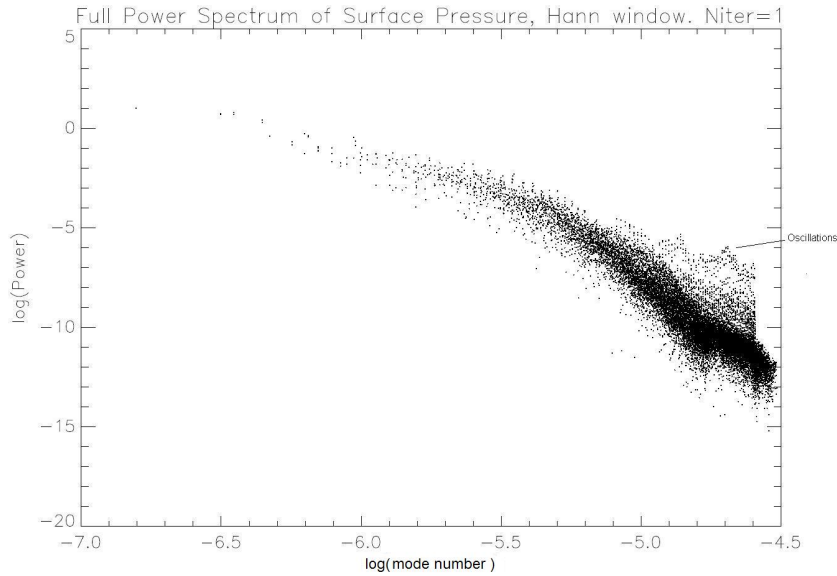


Figure 5.5: Full 1D power series scatter plot, after 1 inner loop iteration, using detrending and the Hann window function.

(figures 2.10a) and b) respectively). We now describe the application of the window functions and the effect they have on our results.

The incremental data was detrended as previously, but now, before the transformation into Fourier space, we multiply the data by a windowing function. From section 2.4 we know that the multiplication of a data set by a rectangular window causes discontinuities to form at the edges of the domain. The hope is that, by applying the smoother window functions, we will remove the discontinuity created by the rectangular window and therefore remove the streaks in the scatter plot.

Figure 5.5 shows the same results as Figure 5.4 but with the multiplication of the detrended incremental data by the 2D Hann window and Figure 5.6 shows the same result, using the Bartlett window rather than the Hann

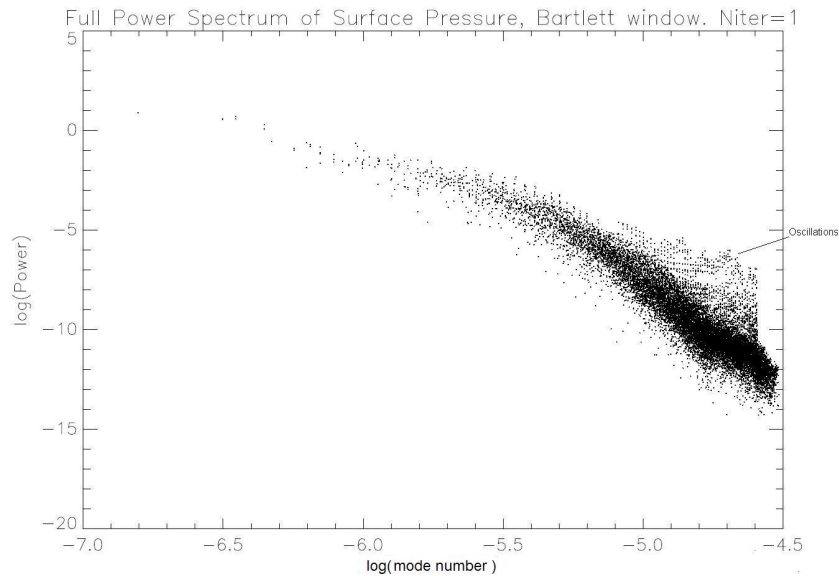


Figure 5.6: Full 1D power series scatter plot, after 1 inner loop iteration, using detrending and the Bartlett window function.

window.

As hoped, the application of the window function to the incremental data has removed the streaking effect almost completely. There are curious oscillations appearing in the results (marked on the graphs), but they do not seem to affect the expected distribution of the results and could well be a product of the fact that we are using ‘real-life’ data which can contain odd phenomena such as this.

Now that we have found a way to remove the effects of aliasing and the increased power in the small scales as a result of this, we can look at a way to accurately display our results and show the evolution of the forecast error.

In the next section we look at producing a 1D periodogram from our 2D plot, by ‘binning’ the mode numbers and plotting the average power against the mid-point mode number in each bin.

5.3 The binned 1D periodogram

To begin with, we approximate the continuous power spectrum using the 2D periodogram. The matrices containing the mode numbers and periodogram information are then reformed into 1D vectors. This is done in such a way that each periodogram value is at the same place in the periodogram vector as its corresponding mode number is in the mode number vector. The mode number vector is then sorted into ascending order. The position of each periodogram value is then rearranged to match the position of its corresponding mode number in the sorted mode number vector. We then group the mode numbers into *bins*, of size p , and calculate the average of each bin. At the same time we bin the periodogram data and plot the average of each periodogram bin against the mid-point of its corresponding mode number bin. This allows us to form a 1D plot of the 2D periodogram to create an approximation to the continuous power spectrum, which also allows us to easily compare the results of different iterations of the inner loop.

After each iteration of the inner loop it is possible for us to form such a plot. By combining these plots together we are able to show the evolution of the power in the incremental data.

Figures 5.7 and 5.8 show the 1D binned periodogram of the incremental data output from the inner loop at iteration numbers 1, 5, 10, 20 and 30, using the Hann and Bartlett windows respectively on the data and with bin size, $p = 100$.

As we can see from both figures, it appears that the forecast error is converging quicker in the larger scales than in the intermediate scales with the smallest scales converging at a rate similar to the large scales.

This appears to correspond with the results by Tanguay et al., [15], and Laroche et al., [9], who also noted that the larger scales converged first. However, they showed that the intermediate scales then converged followed by the smallest scales. Figures 5.7 and 5.8 show that the smallest scales converged before the intermediate scales, indeed, they appear to converge at a similar rate to the larger scales.

The large scale error has converged by the 10th iteration of the inner loop, while the intermediate scales are still to converge completely by the 30th iteration. The smallest scale errors have also converged by the 10th iteration, but it is difficult to draw conclusions about the convergence of the highly oscillatory small scale region in the results.

Clearly, these plots are able to show us the general trends in the evolution of the forecast errors over the minimisation process. We do, however, have one issue with the plots which may cause some question over the validity of our findings, this being the highly oscillatory nature of the power at smaller scales (higher mode number). We are not able to draw accurate conclusions from these results, as it is difficult to accurately describe the evolution of the power in this region.

We are still able, however, to show the evolution of the other scales at a good enough accuracy for conclusions to be drawn.

This region of high frequency error is not present in the results shown in [15] and [9]. One possible explanation for this is that in both papers, the model being used was the simple barotropic vorticity equation and in this project we have used the full nonlinear numerical weather prediction model. The numerical weather prediction model employs a lot of physical approxi-

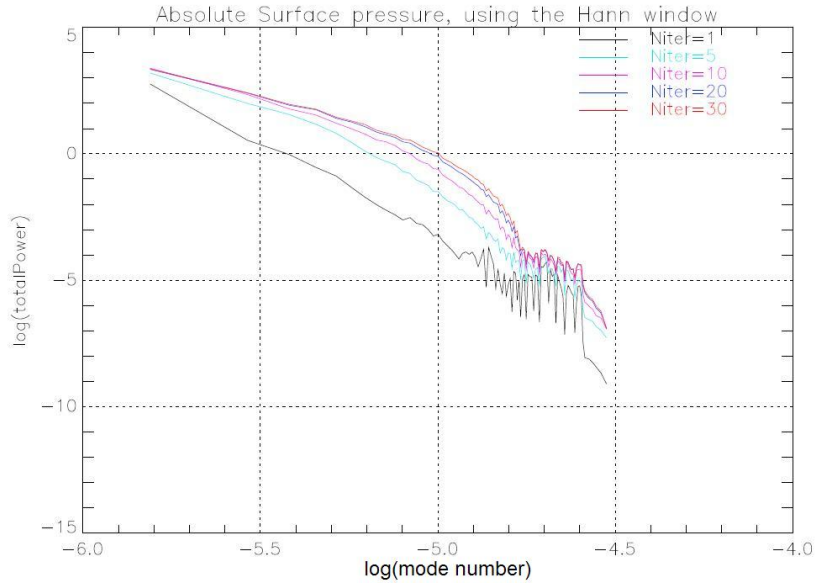


Figure 5.7: Plot showing the binned periodogram data, using the Hann window, of the absolute surface pressure.

mations and is rather more complex than the barotropic vorticity equation. We therefore believe the high frequency region to be an artifact of using the nonlinear model and the ‘real-life’ data it produces.

To further the comparison between the forecast error at the different inner loop iterations, we now looked at producing a relative plot, which involved dividing the absolute plots (Figures 5.5 and 5.6) by the variance of the incremental data at each corresponding iteration. The resultant plot is shown in figure 5.9.

The result displayed is formed by multiplying the incremental data by the Hann window. Since the results from using the Bartlett and Hann window are so similar we present only the Hann window results.

Figure 5.9 allows us to compare the evolution even more accurately be-

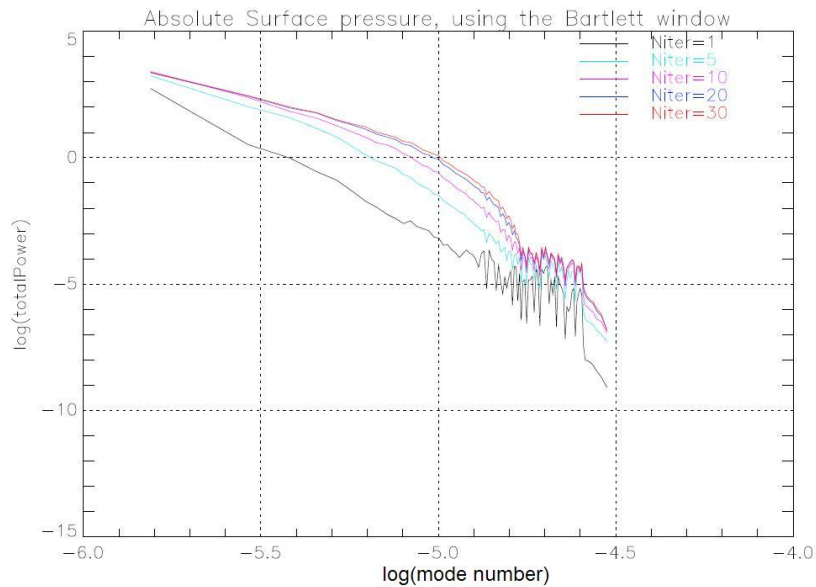


Figure 5.8: Plot showing the binned periodogram data, using the Bartlett window, of the absolute surface pressure.

tween iterations, since the results are now displayed relative to one another. Clearly the relative plot backs up the conclusions drawn from the absolute plots that the larger scales converge before than the intermediate scales, with the smallest scales converging at a similar rate to the largest scales. As we can see, the largest and smallest scales have converged by the 10th iteration with the intermediate scales still to converge at the 30th iteration.

In chapter 6 we conclude by summing up the results obtained in this section and comparing them to previous work. In the next chapter we shall also discuss limitations of our method and what our results mean for future work.

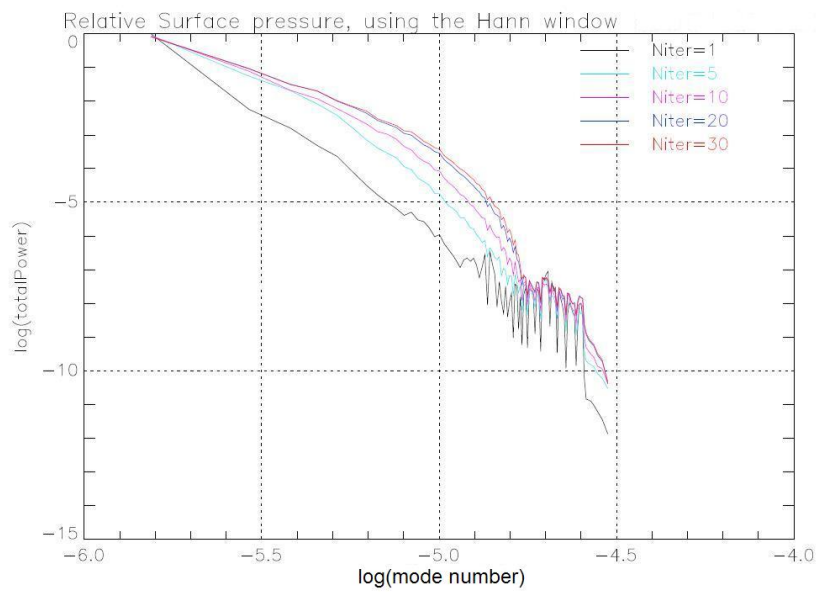


Figure 5.9: Plot showing the binned periodogram data, using the Hann window, of the relative surface pressure.

Chapter 6

Conclusion

In this chapter we draw conclusions based on our results on the evolution of the scales present in the forecast errors of the incremental 4D-Var method, applied to the UK Met Office numerical weather prediction model. We then compare these results to the results of previous pieces of work which used the simple barotropic vorticity equation model.

The work previously conducted on the evolution of scales present in the forecast error was only done using the simple barotropic vorticity equation model. In this project we used the nonlinear numerical weather prediction model in order to produce results never obtained before.

In order to view the evolution of the scales present in the forecast error of the incremental 4D-Var method we transformed the data into Fourier space and subsequently formed a 2D periodogram. We discovered that by manipulating and massaging the data we were able to produce an estimate of the power spectrum of the incremental data.

The manipulated 2D periodogram data was then binned and reformed to produce a 1D binned periodogram, which showed the average power in each

mode number bin plotted against the mid-point mode number value of the corresponding bin.

By looking at the incremental results after 1, 5, 10, 20 and 30 iterations of the inner loop, we were able to study the evolution of the scales present in the forecast error. From this we were able to deduce that the error in the largest scales converged quicker than in the intermediate scales, with the smallest scales converging at a similar rate to the largest scales. The results showed that by the 10th iteration the largest and smallest scale errors had converged but the intermediate scale errors still had not converged by the 30th iteration.

Results by Tanguay et al., [15] and Laroche et al., [9], showed that the largest scales converged first, followed by the intermediate scales then finally the smallest scales. Our results do not so much contradict these results, but nor do they support them completely. We showed that the largest and smallest scales converged at a similar rate, followed by the convergence of the intermediate scales.

The high frequency oscillations located in the small scale region of the 1D plot is believed to be an artifact of us using 'real-life' data, which can never be perfect. We also believe the use of the complicated nonlinear model, which contains much more physical approximations than in the barotropic vorticity equation model, may have caused the odd behaviour in the small scale region. The use of the unified model as opposed to the simple barotropic model is one possible reason why the work by Tanguay et al. and Laroche et al. saw no such high frequency oscillations in the small scale error. We are of course using an operational model, which has been designed to be as accurate as

possible with regards to the physical states, where as the barotropic vorticity equation is a simple model, chosen in both papers due to its relatively well-behaved nature.

We now can now draw some conclusions about the possible use of the multigrid method to speed up the minimisation process. It does not appear that there would be any computational advantage of using a V-cycle multigrid method, because there are small scale errors persisting in the forecast error. However, since the smallest scales converged as fast as the largest scales, with persisting intermediate scales, it may be possible to use the multigrid method on the outer loops. This would involve running the outer loop minimisation at different resolutions, and running the inner loop as usual. For example, it may be possible to run the first outer loop on a lower resolution grid to correct for the larger scales, then run successive outer loops on a higher resolution grids in order to correct for the smaller scales.

Bibliography

- [1] George Arfken (1985) *Mathematical Methods for Physicists*, Miami University, Academic Press, Third Edition, 760-790

- [2] J.S. Bendat. and A.G. Piersol (2000) *Random Data Analysis and Measurement Procedures*, Wiley Interscience, Third Edition, 396-397

- [3] F. Bouttier and P. Courtier (1999) *Data assimilation concepts and methods*. ECMWF Meteorological Training Course Lecture Series, Web resource:-
[http://www.ecmwf.int/newsevents/training/rcourse_notes/](http://www.ecmwf.int/newsevents/training/rcourse_notes/DATA_ASSIMILATION/ASSIM_CONCEPTS/Assim_concepts11.html)
[/DATA_ASSIMILATION/ASSIM_CONCEPTS](http://www.ecmwf.int/newsevents/training/rcourse_notes/DATA_ASSIMILATION/ASSIM_CONCEPTS/Assim_concepts11.html)
[/Assim_concepts11.html](http://www.ecmwf.int/newsevents/training/rcourse_notes/DATA_ASSIMILATION/ASSIM_CONCEPTS/Assim_concepts11.html), last accessed 17/08/06

- [4] K.G. Beauchamp and C.K. Yuen (1979) *Digital Methods for Signal Analysis*, George Allen and Unwin Ltd, 93-95

- [5] R.B. Blackman and J.W. Tukey (1959) *The Measurement of Power Spectra*, Dover Publications, 69-85

- [6] E. Oran Brigham (1988) *The Fast Fourier Transform and its Applications*, Prentice-Hall International, 83-85 and 240-241
- [7] C. Chatfiel (2004) *The Analysis of Time Series - An Introduction*, Chapman and Hall/CRC, Sixth Edition, 126-141
- [8] G. Inverarity, Private Communication, 2006
- [9] S. Laroche and P. Gauthier (1998) *A validation of the incremental formulation of 4D variational data assimilation in a nonlinear barotropic flow*, Tellus (1998), 50A, 557-572
- [10] A. S. Lawless, S. Gratton and N. K. Nichols (2005) *An Investigation of Incremental 4D-Var Using Non-Tangent Linear Models*, Quarterly Journal of the Royal Meteorological Society, Vol. 131, 459-476
- [11] N. K. Nichols (2003) *Data Assimilation: Aims and Basic Concepts*, Published in *Data Assimilation for the Earth System*, by R. Swinbank, V. Shutyaev and W.A. Lahoz, Kluwer Academic, 9-20
- [12] W.H. Press, S.A. Teukolsky, W.T. Vetterling and B.P. Flannery (1992) *Numerical Recipes in Fortran - The Art of Scientific Computing*, Cambridge University Press, Second Edition, 543-545.
- [13] U. Ruede updated by C.C. Douglass (1993) *What are Multigrid Methods?*, 1995, Web resource:-

<http://www.mgnet.org/mgnet/tutorials/xwb/mg.html>, last accessed 17/06/08

- [14] R.B. Stull: *An Introduction to Boundary Layer Meteorology*, Kluwer Academic Publications, 295-313
- [15] M. Tanguay, P. Bartello, and P. Gauthier (1995) *Four-dimensional data assimilation with a wide range of scales*, *Tellus*(1995), 47A, 974-997